crystals

MDPI

Article

Influence of Ce^{3+} on the Structural, Morphological, Magnetic, Photocatalytic and Antibacterial Properties of Spinel $MnFe_2O_4$ Nanocrystallites Prepared by the Combustion Route

Salma A. Al-Zahrani [1,*], A. Manikandan [2,3,*], K. Thanrasu [4], A. Dinesh [4], K. Kanmani Raja [4], M. A. Almessiere [5,6], Y. Slimani [6], A. Baykal [7], S. Bhuminathan [8], S. Raghavendra Jayesh [8], Jahir Ahmed [9], Hajar S. Alorfi [10], Mahmoud A. Hussein [10,11], Imran Khan [12] and Anish Khan [10,13,*]

1 Chemistry Department, Faculty of Science, University of Ha'il, P.O. Box 2440, Ha'il 81451, Saudi Arabia
2 Department of Chemistry, Bharath Institute of Higher Education and Research (BIHER), Chennai 600073, India
3 Centre for Catalysis and Renewable Energy, Bharath Institute of Higher Education and Research (BIHER), Chennai 600073, India
4 Department of Chemistry, Government Arts College for Men (Autonomous), Nandanam, University of Madras, Chennai 600035, India; thanrasuk@gmail.com (K.T.); dinesha1@gmail.com (A.D.); kkanmania@gmail.com (K.K.R.)
5 Department of Physics, College of Science, Imam Abdulrahman Bin Faisal University, P.O. Box 1982, Dammam 31441, Saudi Arabia; malmessiere@uod.edu.sa
6 Department of Biophysics, Institute for Research & Medical Consultations (IRMC), Imam Abdulrahman Bin Faisal University, P.O. Box 1982, Dammam 31441, Saudi Arabia; yaslimani@iau.edu.sa
7 Department of Nanomedicine Research, Institute for Research & Medical Consultations (IRMC), Imam Abdulrahman Bin Faisal University, P.O. Box 1982, Dammam 31441, Saudi Arabia; abaykal@iau.edu.sa
8 Sree Balaji Dental College, Bharath Institute of Higher Education and Research (BIHER), Chennai 600073, India; sbhuminathan@gmail.com (S.B.); raghavendrajs@gmail.com (S.R.J.)
9 Promising Centre for Sensors and Electronic Devices (PCSED), Advanced Materials and Nano-Research Centre, Najran University, P.O. Box 1988, Najran 11001, Saudi Arabia; jahmedsust@gmail.com
10 Chemistry Department, Faculty of Science, King Abdulaziz University, Jeddah 21589, Saudi Arabia; hsalorfi@gmail.com (H.S.A.); mahussein74@yahoo.com (M.A.H.)
11 Chemistry Department, Faculty of Science, Assiut University, Assiut 71516, Egypt
12 Applied Sciences and Humanities Section, University Polytechnic, Faculty of Engineering and Technology, Aligarh Muslim University, Aligarh 202002, India; imrannano@gmail.com
13 Center of Excellence for Advanced Materials Research, King Abdulaziz University, Jeddah 21589, Saudi Arabia
* Correspondence: s.alzahrane@uoh.edu.sa (S.A.A.-Z.); manikandana.che@bharathuniv.ac.in (A.M.); editoranishkhan@gmail.com (A.K.)

check for updates

Citation: Al-Zahrani, S.A.; Manikandan, A.; Thanrasu, K.; Dinesh, A.; Raja, K.K.; Almessiere, M.A.; Slimani, Y.; Baykal, A.; Bhuminathan, S.; Jayesh, S.R.; et al. Influence of Ce^{3+} on the Structural, Morphological, Magnetic, Photocatalytic and Antibacterial Properties of Spinel $MnFe_2O_4$ Nanocrystallites Prepared by the Combustion Route. *Crystals* **2022**, *12*, 268. https://doi.org/10.3390/cryst12020268

Academic Editors: Faheem Ahmed, Nishat Arshi, Shalendra Kumar, Nagih Shaalan, Vladimir I. Zverev and Rajratan Basu

Received: 29 December 2021
Accepted: 31 January 2022
Published: 16 February 2022
Corrected: 2 April 2025

Publisher's Note: MDPI stays neutral with regard to jurisdictional claims in published maps and institutional affiliations.

Copyright: © 2022 by the authors. Licensee MDPI, Basel, Switzerland. This article is an open access article distributed under the terms and conditions of the Creative Commons Attribution (CC BY) license (https://creativecommons.org/licenses/by/4.0/).

Abstract: The present work describes the effect of Ce^{3+} ion doping on the structural, morphological, and magnetic properties of spinel manganese ferrite ($MnFe_2O_4$) nanocrystallites (NCs) using various instrument techniques. Rare earth element (REE) Cerium (Ce^{3+}) doped $MnFe_2O_4$ NCs were prepared by a simple microwave combustion technique. In the present scenario, ferrites are widely used for photocatalytic dye degradation and antibacterial applications. Aiming to achieve this, we prepared Ce^{3+} doped $MnFe_2O_4$ NCs by microwave combustion method and urea as burning agent and the obtained powder samples were characterized by powder X-ray diffraction (XRD), Fourier transform infrared (FT-IR), high resolution scanning electron microscope (HR-SEM), high resolution transmission electron microscope (HR-TEM) and vibration sample magnetometer (VSM) techniques. The pure spinel phase formation was confirmed by XRD analysis. FTIR spectra show two prominent absorption bands under 1000 cm^{-1}, which confirms the formation of the spinel structure. HR-SEM and HR-TEM pictures demonstrated a sphere-shaped morphology and also expose the combination and agglomeration of grains, which are mostly due to the magnetic characteristics of the samples. The magnetic properties of the synthesized $MnCe_xFe_{2-x}O_4$ (x = 0.0, 0.1, 0.3, and 0.5) NCs were studied by VSM analysis at room temperature (RT) shows ferromagnetic behavior. The photodegradation results showed that $MnFe_2O_4$ and Ce doped $MnFe_2O_4$ NCs have a higher potential to degrade methylene

blue (MB) and the sample $MnCe_{0.3}Fe_{1.7}O_4$ NCs showed superb photocatalytic performance (91.53%) compared to other samples. The antibacterial activities of Gram-positive *S. aureus*, *B. subtilis* and Gram-negative *K. pneumonia* and *E. coli* were investigated using pure and Ce^{3+} substituted $MnFe_2O_4$ NCs and a higher activity for $MnCe_{0.3}Fe_{1.7}O_4$ NCs than other samples was observed, which indicated that they can be used in biomedical applications.

Keywords: Ce^{3+} substituted $MnFe_2O_4$; magnetic nanoparticles; organic dyes; photocatalysis; efficiency

1. Introduction

Spinel ferrites (AFe_2O_4, where A = Ni, Cu, Mg and Zn, etc.) are a well-known family of scientific materials and have been well studied owing to their unique magnetic properties, as they are endowed with high electrical resistivity [1–5]. The excellent properties of spinel ferrites are well utilized in modern technological applications. Ferrites often have a spinel structure with the formula AB_2O_4, where A and B are various metal cations, with iron being the most common (Fe). Spinel ferrites typically adopt FCC oxides (O^{2-}) with A cations reside in one-eighth of the tetrahedral holes and B cations reside in half of the octahedral holes, i.e., instead of the normal spinel structure, ferrite crystals have the inverse spinel structure: B cations occupy (one-eighth of the tetrahedral holes, A cations occupy one-fourth of the octahedral sites, and B cations occupy the remaining one-fourth octahedral sites. Spinel ferrites with a mixed structure can also be possible with the formula $[M_{1-\delta}{}^{2+}\ Fe_{\delta}{}^{3+}][M\delta\ {}_{2+}Fe_{2-\delta}{}^{3+}]O_4$, where δ represents the degree of inversion [6–10]. Additionally, ferrites are hard and brittle, contain iron, are generally grey or black, and are polycrystalline materials. They can be magnetized or drawn to a magnet since they are ferrimagnetic. Conflicting with other ferromagnetic materials, most of the ferrites are insulating materials, making them ideal for transformers to defeat eddy currents for applications such as magnetic cores [11–15]. Spinel ferrites have vast applications in the present technological world. The main applications are precursors for ferro-fluids, radio, magnetic guided drug-delivery agents, telecommunication, biomedicine, magnetic storage, gas sensor, television, microwave, military devices, microwave absorbers, satellite communication, humidity sensors and magnetic storage [16,17].

Among them, manganese ferrite ($MnFe_2O_4$) is an important material with good chemical stability, moderate magnetization, high sensitivity, band gap of ~2.0 eV, and high electrical resistivity, and it is widely used in the transformer core, gas sensor, anode materials, photocatalysis, microwave absorber, and magnetic hyperthermia applications [18]. $MnFe_2O_4$ nanoparticles exhibit a spinel cubic structure. Manganese ferrite ($MnFe_2O_4$) is a kind of lenient magnetic material among different ferrites with little saturation magnetization (Ms) and coercivity (Hc). They are used for sensing gases and temperature, and for catalytic applications. $MnFe_2O_4$ nanoparticles have been shown to be superparamagnetic or ferrimagnetic depending on its size. $MnFe_2O_4$ nanoparticles with a size smaller than 15 nm behave as a superparamagnetic material and those above 15 nm behave as ferrimagnetic materials. The oxygen atoms in ferrites surround the metal ions, resulting in a super exchange interaction between the A- and B-sublattices, which disturbs the ferrites' magnetic properties [19]. These interesting properties motivated us to choose $MnFe_2O_4$ magnetic nanoparticles for the present study.

The bulk $MnFe_2O_4$ crystallizes mostly in a normal spinel structure with interstitial sites, such as A- and B-sites. Among the two sites, the manganese ions occupy the A-sites, whereas the iron ions occupy the B-sites [20]. Compared with the bulk form, nanocrystalline ferrites exhibit unusual behaviors, such as metastable cation distribution, super paramagnetism, enhanced coercivity and improved electrical resistivity [21]. Hence, the preparation and performance evolution of nanocrystalline ferrites attract increasing scientific attention. Additionally, the surface area and crystallite size of the ferrites are leads to the properties of the materials. It is reported that the replacement of Fe by other elements, such as Ce,

La, Al, etc., occupies the B sites and modifies the magnetic and electrical properties of $MnFe_2O_4$ [22].

The great effort made by previous studies demonstrates that the substitution of Ce for Fe in $MgFe_2O_4$ effectively tunes the size of the crystallites, enhances the magnetization, and alters the electrical properties [23]. Since the preparation method plays a dominant role in deciding the size of the crystallites and its properties, in the present work we intend to synthesize nanocrystalline $MnCe_xFe_{2-x}O_4$ ferrites using a microwave combustion method, which is not reported in earlier literature surveys. The present method is practically efficient, due to the short reaction time and a relatively low temperature of processing.

In recent years, many physical and chemical methods have been used to synthesize nanosized ferrites. Because their composition and microstructure influence their structural, magnetic, and electrical properties, they are vastly reliant on the preparation method and conditions. R. Foroutan et al. reported the adsorption properties of montmorillonite (MMT) using graphene oxide (GO) and $CoFe_2O_4$ magnetic nanoparticles for methyl violet (MV) removal. They observed that the MMT/GO/$CoFe_2O_4$ magnetic composite demonstrates the high adsorption capacity and suitable reusability toward MV removal from aqueous media [24]. M. M. Boushehrian et al. reported a new nanocomposite of kaolin/copper iron oxide ($CuFe_2O_4$), which were used to remove cationic dyes of methylene blue (MB) and methyl violet (MV) from an aqueous media in a batch system. They observed that, under the optimal conditions, the removal efficiency of MB and MV dyes using a kaolin/$CuFe_2O_4$ nanocomposite was obtained with values of 98.64% and 99.25%, respectively, which show the highest removal ever achieved for MB and MV [25]. Additionally, the elimination of methyl violet dye (MVD) and Nile blue dye (NBD) from a water solution using a CNT/MgO/$CuFe_2O_4$ magnetic composite powder produced by co-precipitation was investigated. The magnetic composite powder could be used several times in the adsorption process of MVD and NBD without a significant reduction in removal efficiency. The results showed that the CNT/MgO/$CuFe_2O_4$ magnetic composite powder can be successfully used in textile wastewater treatment [26].

R. Foroutan et al. reported activated carbon oak wood (ACOW600) and modified activated carbon using ZnO (ACOW600/ZnO) and Fe_3O_4 (ACOW600/ZnO/Fe_3O_4) nanoparticles were used to remove methyl violet 2B dye (MV2B) from aqueous solutions. Textile wastewater was significantly treated by ACOW600, ACOW600/ZnO, and ACOW600/ZnO/Fe_3O_4 adsorbents. The recycling of the adsorbents was demonstrated that the investigated adsorbents could be re-utilized many times in the MV2B removal process [27]. Additionally, a new nanocomposite, clinoptilolite (CLT)/Starch/$CoFe_2O_4$, was synthesized using the co-precipitation method. The prepared magnetic composite powder was utilized for the decontamination of methylene blue dye (MBD), methyl violet dye (MVD), and crystal violet dye (CVD) from water media. The maximum adsorption capacity of CVD, MBD, and MVD to the desired composite was determined as 32.84 $mg \cdot g^{-1}$, 31.81 $mg \cdot g^{-1}$, and 31.15 $mg \cdot g^{-1}$, respectively. Finally, the ad(de)sorption experiments' results showed that the synthesized nanocomposite adsorbent has an excellent ability to adsorb cationic dyes after several consecutive cycles [28].

Among all the spinel ferrite systems, rare earth element (REE) doped $MnFe_2O_4$ are soft materials called ferromagnetic materials. Furthermore, these materials have attractive magnetic properties, such as large M_s, low H_c, moderate M_r, remarkable Y-K angle, high initial permeability, high electrical resistivity, and low energy loss. REE doped $MnFe_2O_4$ NPs are widely used in scientific applications, such as spintronic systems and data transfer circuits as magnetic wave absorbers, converters, and inductor cores [29]. The concentration of Ce^{3+} in the host material is expected to enhance structure properties. By incorporating different cations into the crystal structure, it is possible to tune the catalytic response of $MnFe_2O_4$ nanoparticles. Due to the higher spin–orbit pairing in their 4f electrons, REE ions with massive ionic radii experience strong magnetostriction, magnetic moments, and magneto-crystalline anisotropy at low temperatures [30–32]. Replacing trivalent iron with REE ions at the Fe site improves dielectric, structural, optical, sensing and magnetic

phenomena in $MnFe_2O_4$ NPs. There have been several studies on the integration of REE ions into $MnFe_2O_4$ NPs [33–35].

Ceramics, polymers, and organic compounds can be used to make photocatalytic materials. Photocatalytic materials with low hysteresis and high stability are improving their efficiency and are reusable [36]. In terms of high mechanical strength, mechanical and chemical stability, low cost and operability in a wide range of catalyst are found to be a better alternative to all other nanocatalytic materials [37,38]. To the best of our knowledge, only a limited number of articles discussed the influence of cerium ions on the morphology, crystal structure, and magnetic properties of $MnFe_2O_4$ NCs. In the present work, for the first time, we investigate the structural, morphological, and photocatalytic properties of Ce^{3+} doped $MnFe_2O_4$ NCs and the obtained results are reported in detail.

2. Experimental Procedure

2.1. Synthesis of Spinel $MnCe_xFe_{2-x}O_4$ Nanocrystallites

Spinel $MnCe_xFe_{2-x}O_4$ nanocrystallites were synthesized using the corresponding nitrates of metals $Mn(NO_3)_2{\cdot}6H_2O$ (manganese nitrate), $Fe(NO_3)_3{\cdot}9H_2O$ (ferric nitrate), and $Ce(NO_3)_3{\cdot}6H_2O$ (cerium nitrate), and urea was used as the fuel. Here, urea acted as fuel, whereas the precursors of metal nitrates (manganese, ferric and cerium nitrates) functioned as oxidizers. The chemicals were brought from SD fine (India) and were of systematic grade and utilized as usual. For pure manganese ferrite, the precursors of manganese nitrate and ferric nitrate were mixed by a continuing molar ratio 1:2 and dissolved in double distilled water. Urea was added to the main achieved solutions and agitated for 1 h and the final obtained homogeneous substances were transported to a silica crucible and were placed in a microwave oven (SAMSUNG, Noida, India), utilized as the mechanism of treatment. The microwave oven power was set as 900 W for 10 min (2.54 GHz). Under the influence of microwave energy (ME), the solutions were subjected to the following procedures: steaming, vaporization, desiccation, and finally decomposition; this caused the progression of the reaction gas and an explosion took place, which ground the speedy flame feathery construction of pure $MnFe_2O_4$. Similarly for the preparation of Ce^{3+} doped $MnFe_2O_4$ NCs, cerium nitrate was added by a stoichiometry ratio. Additionally, products were splashed by water and ethanol, then dried at 70 °C for 30 min. The obtained samples, viz., x = 0.0, 0.1, 0.3 and 0.5, were labeled as $MnFe_2O_4$, $MnCe_{0.1}Fe_{1.9}O_4$, $MnCe_{0.3}Fe_{1.7}O_4$ and $MnCe_{0.5}Fe_{1.5}O_4$ NCs, respectively.

2.2. Characteri Zation Techniques

Powder X-ray (Model Rigaku Ultima III, Tokyo, Japan) was used to authorize the phase formation by employing CuKα energy (λ= 1.5406 Å) and within 2θ series of 20–80°. The morphological and elemental analysis was recorded using scanning electron microscope accompanied by FEI Quanta FEG 200 (Hillsboro, OR, USA). The transmission electron micrographs were carried out by Philips-TEM (CM20, Brussels, Belgium). Perkin Elmer spectrophotometer (Spectrum RX1, Los Altos, CA, USA) was utilized to log the FTIR spectra. Lake Shore (Model7404, Westerville, OH, USA) vibration sample magnetometer (VSM) equipped with 3 magnets is used to perform magnetization measurements at RT.

2.3. Photocatalytic Evaluation

The photocatalytic performances of $MnFe_2O_4$, $MnCe_{0.1}Fe_{1.9}O_4$, $MnCe_{0.3}Fe_{1.7}O_4$ and $MnCe_{0.5}Fe_{1.5}O_4$ NCs were examined under a visible light (Xenon lamp 300 W; $\lambda > 400$ nm) treatment. The photocatalytic activity was analyzed at RT. Exactly 100 mg of the nanocatalyst was distributed in 100 mL of methylene blue (MB) (10 mg/L), which was reserved in a quartz glass photocatalytic reactor. Before irradiation, the aliquot was stirred 30 min in dark conditions and it was ensured that the catalyst equilibrium of adsorption–desorption was reached between the dye and photocatalyst. The degradation efficiency was examined using UV absorption readings, which lead to govern the dye absorptions at a certain

time interval. The photo-catalytic performance of the pure $MnFe_2O_4$ and cerium doped $MnFe_2O_4$ NCs at various percentages was also investigated.

2.4. Antibacterial Activity

The antibacterial action (ABA) of $MnFe_2O_4$, $MnCe_{0.1}Fe_{1.9}O_4$, $MnCe_{0.3}Fe_{1.7}O_4$ and $MnCe_{0.5}Fe_{1.5}O_4$ NCs was examined by the human pathogens (HPs) Gram-positive *S. aureus* and *B. subtilis*, and Gram-negative *K. pneumonia* and *E. coli*. An immediate culture of all microbes was performed and wiped onto MH (Mueller Hilton) agar dishes. By a CB, hovels were embossed on agar, monitored by adding $MnFe_2O_4$, $MnCe_{0.1}Fe_{1.9}O_4$, $MnCe_{0.3}Fe_{1.7}O_4$ and $MnCe_{0.5}Fe_{1.5}O_4$ (10 µg/mL). Dishes were nurtured at 37 °C/24 h and zone of reserves on the HPs were distinguished by diameter.

3. Results and Discussion

3.1. Structural Analysis

Figure 1 illustrates an X-ray diffractogram (XRD) of the spinel $MnCe_xFe_{2-x}O_4$ (x = 0.0, 0.1, 0.3 and 0.5) NCs in the 2θ range of 20–80° at RT. With the presence of narrow and high diffraction peaks, the patterns show good crystallinity. The existence of high diffraction peaks corresponding to crystal planes (111), (220), (311), (222), (400), (422), (511), and (442) indicate that the cubic spinel phase is present. The XRD analysis shows the formation of a single-phase spinel structure having Fd-3m space group [39]. The lattice parameter increases with dopant concentration, reaching the limit of 8.388 Å as shown in Table 1. Scherrer's formula was used to measure the average crystallite size of the as synthesized samples between 22 and 24 nm in size. The values of lattice parameter and crystallite size are shown in Table 1.

Table 1. The lattice parameter (a, Å) and crystallite size (L, nm) of spinel $MnCe_xFe_{2-x}O_4$ (x = 0.0, 0.1, 0.3 and 0.5) NCs.

Sample Code	*L* (nm) by Debye Scherrer	*D* (nm) by Williamson–Hall Plot	*a* (Å)
$MnFe_2O_4$	26.48	27.13	8.359
$MnCe_{0.1}Fe_{1.9}O_4$	25.76	26.47	8.362
$MnCe_{0.3}Fe_{1.7}O_4$	23.98	24.56	8.375
$MnCe_{0.5}Fe_{1.5}O_4$	24.33	25.84	8.386

To deduce the lattice parameter of the $MnFe_2O_4$ and Ce:$MnFe_2O_4$ NCs, Equation (1) was used.

$$a = d_{hkl}\sqrt{(h^2 + k^2 + l^2)} \quad (1)$$

where d_{hkl} is the inter-atomic space consistent to *h*, *k*, and *l* planes (Miller indices), respectively, and *a* is the lattice constant. Lattice parameter '*a*' resembles the spinel cubic structure (Figure 2). The lattice parameter '*a*' value was calculated for $MnFe_2O_4$ and Ce doped $MnFe_2O_4$ NCs and it was found to be 8.348 Å and 8.388 Å, respectively [40]. The increase of '*a*' is due to doping of larger ionic size Ce ions (0.92 Å) in place of the lower ionic size Fe cations (0.67 Å), which obeys Vegard's law [41–43].

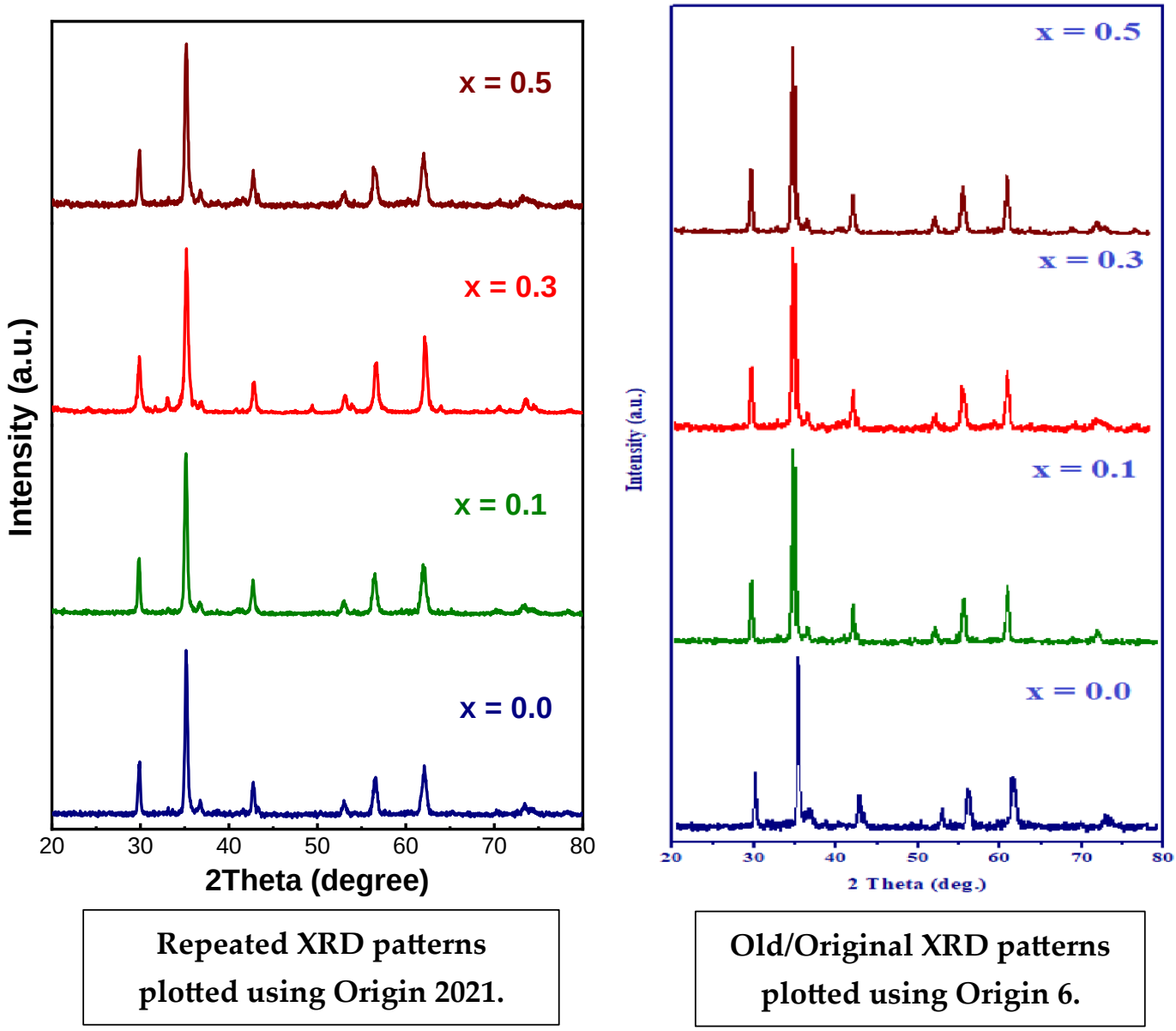


Figure 1. Powder XRD patterns of spinel $MnCe_xFe_{2-x}O_4$ (x = 0.0, 0.1, 0.3, and 0.5) NCs.

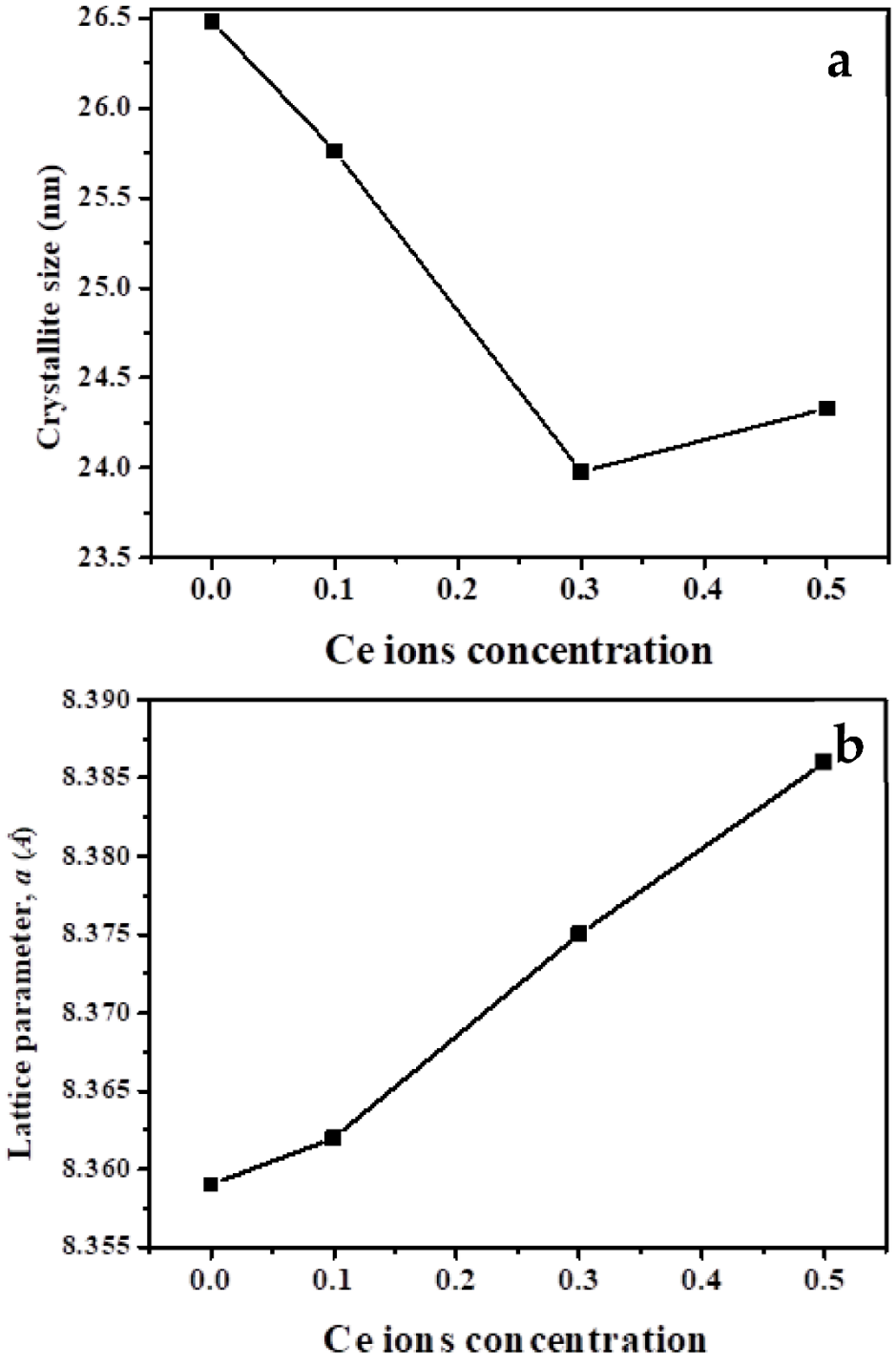


Figure 2. Crystallite size (**a**) and lattice constant (**b**) values of spinel $MnCe_xFe_{2-x}O_4$ (x = 0.0, 0.1, 0.3 and 0.5) NCs.

The particle size (D) was obtained by employing the Williamson–Hall (W–H) plot, as shown in Equation (2):

$$\frac{\beta \cos\theta}{\lambda} = \frac{k}{D} + \frac{4\varepsilon \sin\theta}{\lambda} \quad (2)$$

where k is the constant and strain associated with samples signified by ε. The W–H plot is $4\sin\theta/\lambda$ vs. $\beta\cos\theta/\lambda$, wherever the interrupt (k/D) is used to control the actual D. The W–H plot for $MnFe_2O_4$ and Ce doped $MnFe_2O_4$ NCs is represented in Figure 3 and the D size attained by the W–H plot method is greater when compared with the L size obtained

by the Scherer method. The variance is, chiefly, due to participation of the strain module in the plot of the W–H route. It can be perceived that, with the increase in Ce ions (x), the L size shrinks, whereas an escalation in the '*a*' can also be detected.

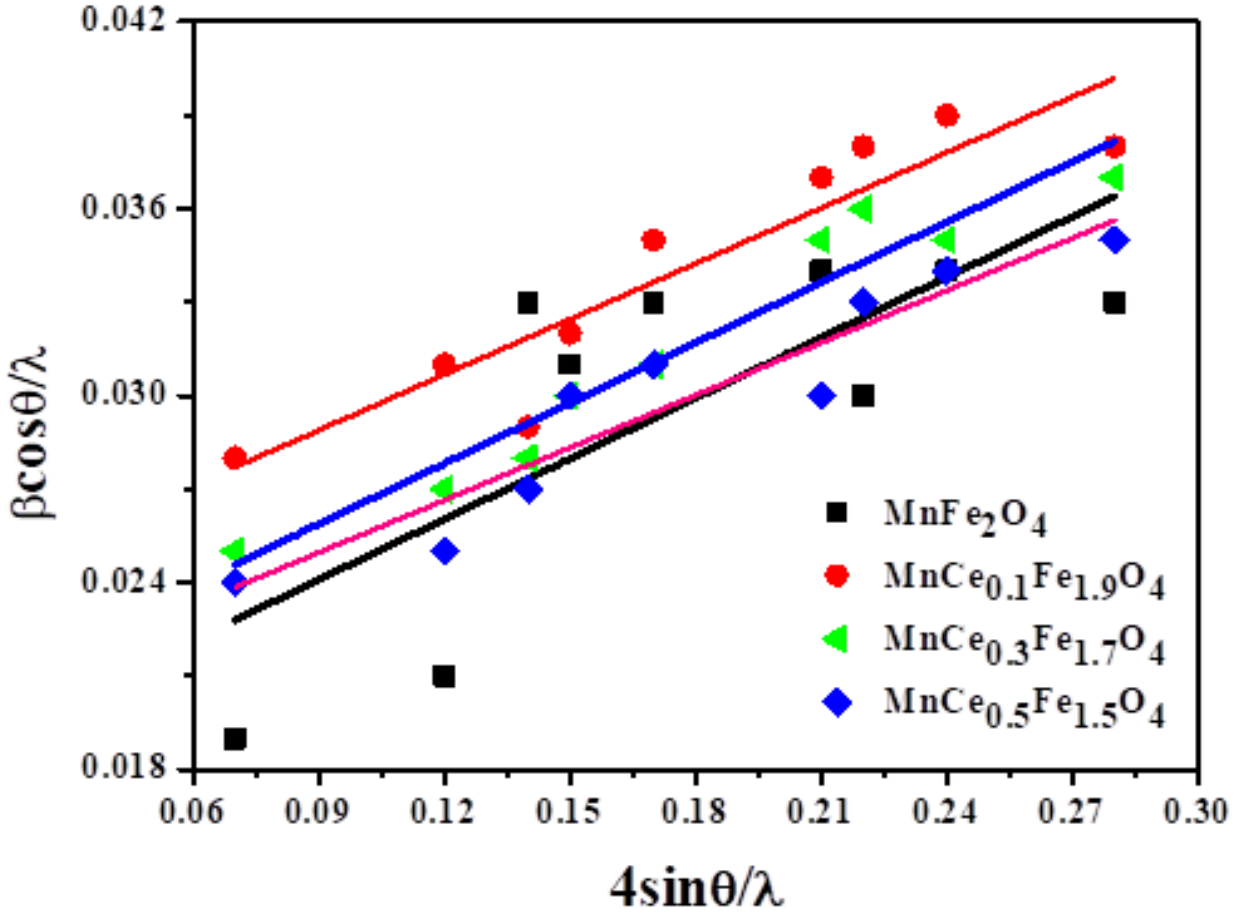


Figure 3. W–H plots of spinel $MnCe_xFe_{2-x}O_4$ (x = 0.0, 0.1, 0.3 and 0.5) NCs.

3.2. Fourier Transform Infrared (FT-IR) Spectral Analysis

To better understand the presence of metal–oxygen (M–O) in these materials, FTIR studies of $MnCe_xFe_{2-x}O_4$ (x = 0.0, 0.1, 0.3, and 0.5) NCs were conducted, as shown in Figure 4. In the literature, the absorption band seen at a higher wavenumber (575 cm^{-1}) is relegated to the metal–oxygen (M–O) bond in A-sites, while the absorption band seen at a lower wavenumber (437 cm^{-1}) is the metal–oxygen bond in B-sites. In the 500–600 cm^{-1} frequency range, all ferrites studied in this study have a broad, intense absorption band. Due to the statistical distribution of Mn^{2+}, Ce^{3+} and Fe^{3+} ions at A- and B-sites, band broadening is usually seen in inverse spinel ferrites. As a result, the higher wavenumber band corresponds to M–O vibrations in A-site, while the lower wavenumber band corresponds to M–O vibrations in B-site and the obtained results concur well with the literature on these kind of ferrites [44–46]. In the spectrum of $MnCe_xFe_{2-x}O_4$, a broad peak approximately in the 3400–3500 cm^{-1} region was designated due to the stretching vibration of the OH groups by the water molecule adsorbed on the catalyst surface during handling. Small peaks at 2926 and 2851 cm^{-1} are associated with the C–H stretching vibration. The C–O stretching vibration on the samples is attributed to the small peaks at 1638 and 1412 cm^{-1}. The small peaks at 1012–1210 cm^{-1} correspond to the vibration of spinel structure. The M–O stretching of octahedral (B-) sites is caused due to the bands at 437 cm^{-1}. The M–O stretching at the tetrahedral (A-) sites of the spinel is due to the band at 575 cm^{-1}.

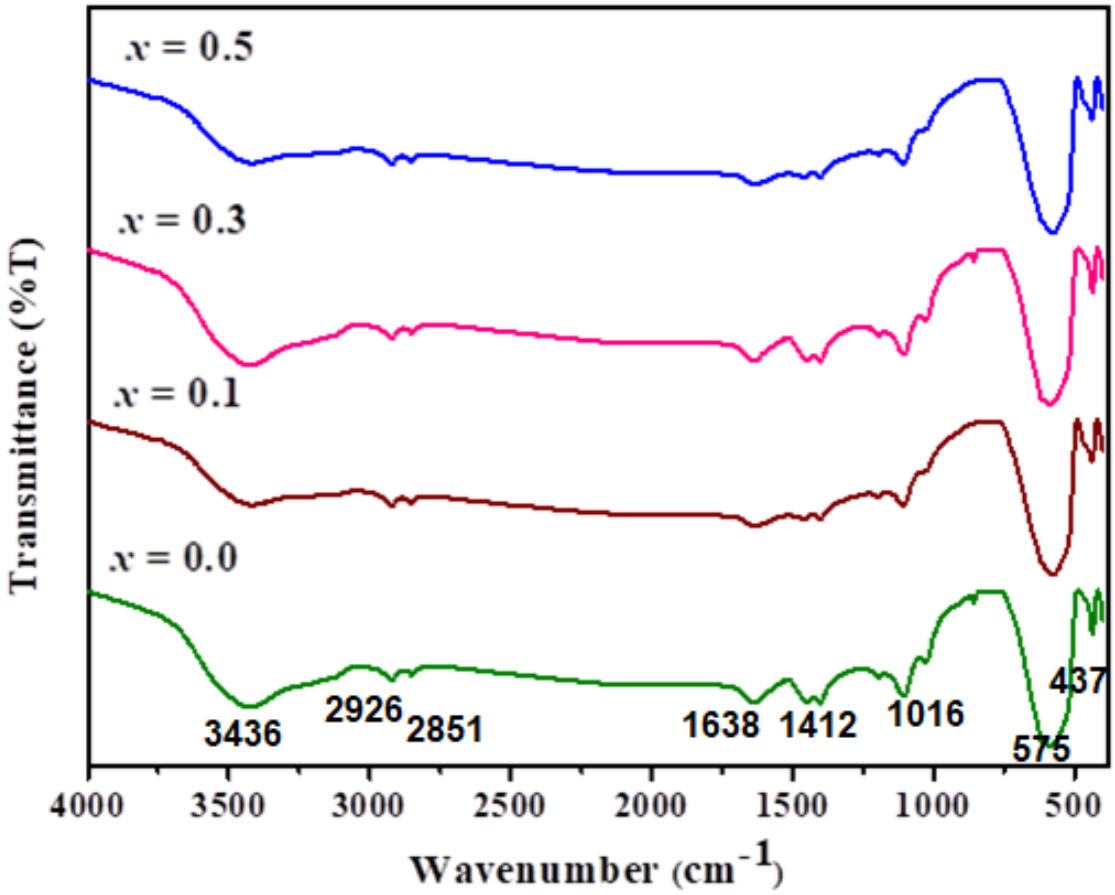


Figure 4. FT-IR spectra of spinel $MnCe_xFe_{2-x}O_4$ (x = 0.0, 0.1, 0.3 and 0.5) NCs.

3.3. HR-SEM Analysis

The study of the surface morphology of spinel $MnFe_2O_4$ and the morphology of the Ce doped $MnFe_2O_4$ NCs was achieved with the aid of HR-SEM analysis. The obtained SEM pictures of $MnFe_2O_4$ (Figure 5a) and Ce doped $MnFe_2O_4$ NCs (Figure 5b,c), respectively, demonstrated a sphere-shaped morphology and also exposed a combination and agglomeration of grains. An agglomerated and sphere-shaped morphology was noticed, which is mostly due to the magnetic characteristics of the samples [47,48]. The surface of Ce doped $MnFe_2O_4$ ferrites shows the agglomerated coalescence behavior. Furthermore, it can be seen that the Ce substitution in $MnFe_2O_4$ NCs influence the surface morphology of nanocrystalline $MnCe_xFe_{2-x}O_4$ NCs.

3.4. HR-TEM Analysis

To find additional confirmation on the nano-scaled samples, an HR-TEM study was performed and is shown in Figure 6a,b. In order to investigate the particle size and shape and nanostructure, the HR-TEM analysis was executed for $MnFe_2O_4$ NCs (Figure 6a) and $MnCe_{0.3}Fe_{1.7}O_4$ NCs (Figure 6b). HR-TEM photographs of the samples clearly show spherical-shaped particles in the manner of nanostructures. Crystallographic clarifications were performed by SAED patterns of $MnCe_xFe_{2-x}O_4$ NCs (x = 0.3) as shown in Figure 6c. A regular of significant Debye rings agreeing to the planes *hkl*; 311, 400, 511, and 440 of the $MnFe_2O_4$ cubic crystal structure indexed a test of the purity and crystallinity of the products. The Debye rings appeared incessant and diffused, and they also had an evidently visible agreement with good crystallinity, which show additional leaflets that demonstrate that the products are very much in the nano regime and well-developed nanoparticles. The images demonstrate that the spherical-shaped $MnCe_xFe_{2-x}O_4$ NCs are aggregated and differences were observed among the surface of the samples.

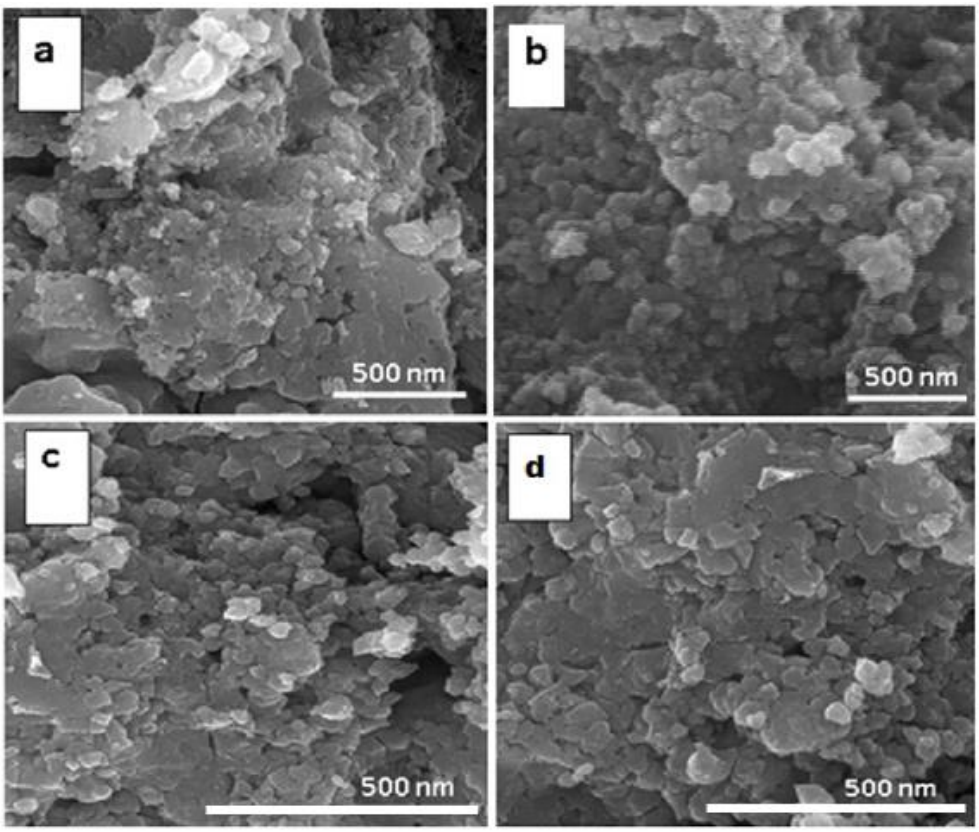


Figure 5. HR-SEM images of (**a**) $MnFe_2O_4$ and (**b**) $MnCe_{0.3}Fe_{1.7}O_4$. (**c**,**d**) Different magnifications of $MnFe_2O_4$ NCs.

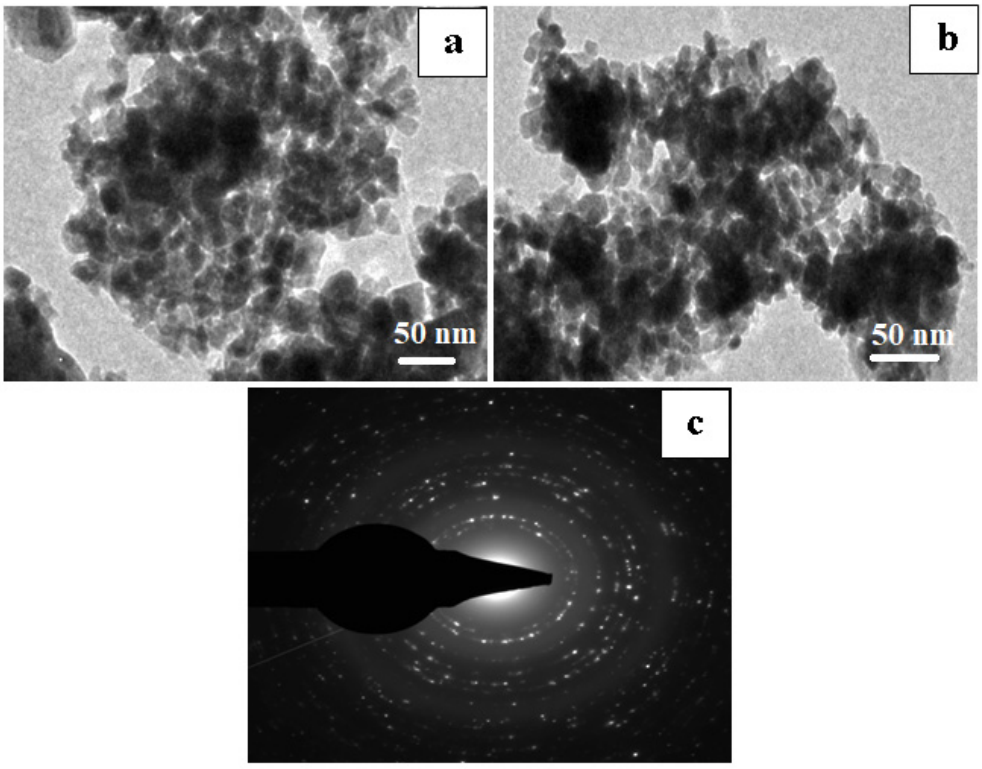


Figure 6. HR-TEM images of (**a**) $MnFe_2O_4$, (**b**) $MnCe_{0.3}Fe_{1.7}O_4$ and SAED pattern of (**c**) $MnCe_{0.3}Fe_{1.7}O_4$ NCs.

3.5. Magnetization Analysis

The magnetic properties of the synthesized magnetic nanoparticles were studied using a vibrating sample magnetometer (VSM) at RT. The magnetic parameters of $MnFe_2O_4$ and Ce doped $MnFe_2O_4$ NCs were undertaken at the field of −15kOe to +15kOe by VSM techniques and the obtained results of magnetization (M) vs. external field (H) plots are shown in Figure 7. The M_s, H_c, and M_r were also determined and are shown in Table 2 [49,50]. The increasing trend in M_s, H_c, and M_r was described on the basis of cerium substitution for prescribed nanoferrites and this fluctuation in values is due to the ionic size and electronic structure of Ce^{3+} ions. Spinel $MnFe_2O_4$ NCs exhibited ferromagnetism. The H_c of $MnFe_2O_4$ and Ce doped $MnFe_2O_4$ NCs were found to lie within the range of 260.72 Oe to 298.25 Oe. The H_c value is primarily organized by its influences, such as high anisotropy and cationic rearrangement [51,52]. From the M–H hysteresis loop, the M_r values of pure and Ce doped $MnFe_2O_4$ NCs were 5.757 emu/g (x = 0), 6.362 emu/g (x = 0.1), 7.521 emu/g (x = 0.3) and 8.533 emu/g (x = 0.5), whose values were dependent on the grain size and structural shape of $MnFe_2O_4$. From the M–H loop, the M_s values for $MnFe_2O_4$ and Ce doped $MnFe_2O_4$ NCs were found to be within the range of 17.86 to 31.22 emu/g. With a smaller crystallite size (specific surface area becomes relatively higher), and once the magnetic field (H) is applied, it is easier to change the direction of magnetic domains, leading to a higher coercive field. In other words, the size effects in nanostructured materials could increase in M_s value. The existence of magnetic layers on the surfaces of materials and the effects of spin canting within the whole volume of the samples can produce a development in M_s value.

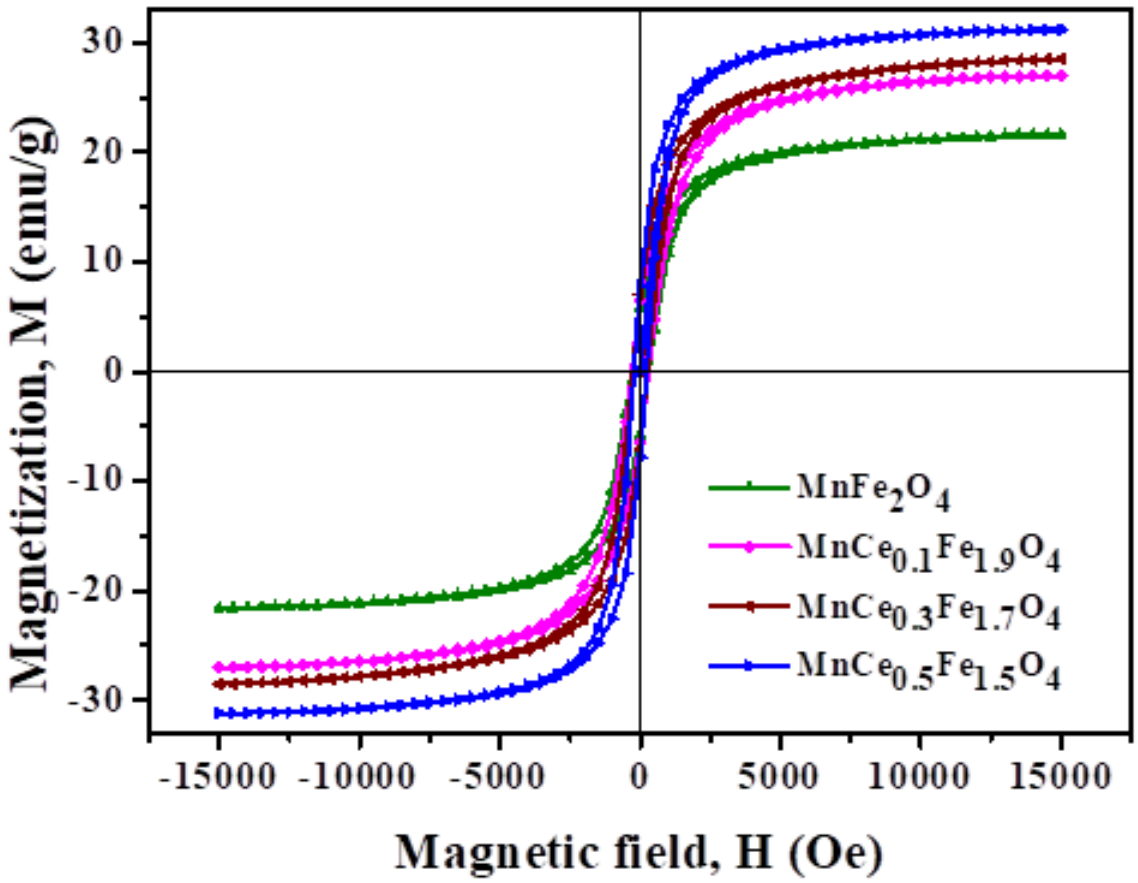


Figure 7. M–H hysteresis loops of spinel $MnCe_xFe_{2-x}O_4$ (x = 0.0, 0.1, 0.3 and 0.5) NCs.

Table 2. Remnant (M_r), Coercivity (H_c), and saturation (M_s) values of spinel $MnCe_xFe_{2-x}O_4$ (x = 0.0, 0.1, 0.3 and 0.5) NCs.

Sample Code	H_c, (O_e)	M_s (emu/g)	M_r (emu/g)
$MnFe_2O_4$	260.72	17.86	5.757
$MnCe_{0.1}Fe_{1.9}O_4$	278.65	24.39	6.362
$MnCe_{0.3}Fe_{1.7}O_4$	292.44	27.65	7.521
$MnCe_{0.5}Fe_{1.5}O_4$	302.25	31.22	8.533

3.6. Photocatalytic Studies

Spinel $MnFe_2O_4$ and Ce doped $MnFe_2O_4$ NCs were examined towards the adsorption–desorption equilibrium that was reached in 30 min, towards the photocatalytic degradation (PCD) of methylene blue (MB) under visible light treatment [53,54]. The PCD efficiency rates of C/C_0 (%) vs. time for MB are shown in Figure 8. The photocatalytic constancy of the blank solution under visible light treatment was calculated in the nonappearance of $MnFe_2O_4$ and Ce doped $MnFe_2O_4$ NCs over 120 min, resulting in a PCD efficiency of 5.85%. The PCD efficiency of the MB solution using $MnCe_{0.3}Fe_{1.7}O_4$ NCs showed a higher degradation percentage (91.53%) than other samples (Table 3).

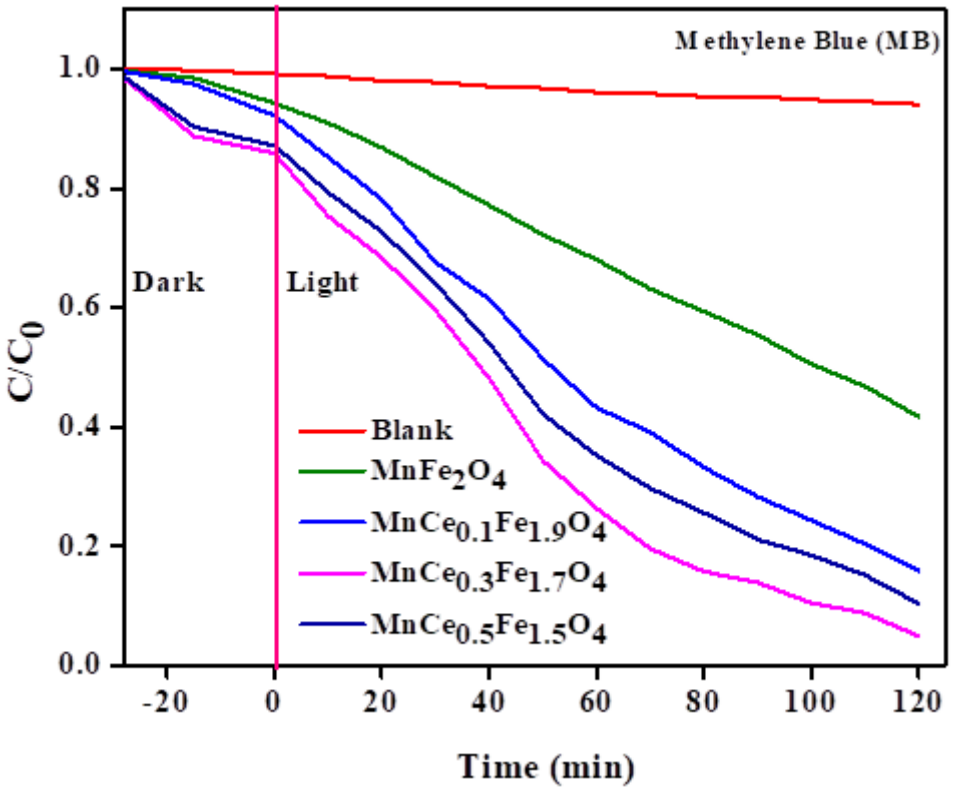


Figure 8. MB dye degradation using spinel $MnCe_xFe_{2-x}O_4$ (x = 0.0, 0.1, 0.3 and 0.5) NCs.

Table 3. Percentage of PCD of MB on to spinel $MnCe_xFe_{2-x}O_4$ (x = 0.0, 0.1, 0.3 and 0.5) NCs.

Sample	MB Dye Degradation Efficiency (%)
Blank	5.85
$MnFe_2O_4$	68.66
$MnCe_{0.1}Fe_{1.9}O_4$	78.95
$MnCe_{0.3}Fe_{1.7}O_4$	91.53
$MnCe_{0.5}Fe_{1.5}O_4$	88.56

3.7. Kinetic Studies

The photocatalytic degradation (PCD) kinetic rate value of MB dye, PCD study of $MnFe_2O_4$ and Ce doped $MnFe_2O_4$ NCs and can be signified by the pseudo-first-order equation:

$$-\ln(Ct/C_0) = k_{abs}(t) \quad (3)$$

where Ct = concentration of MB at different time (t); C_0 is the initial dye attentiveness; and k_{abs} is the pseudo-first-order rate constant (Figure 9). It should be noted that $MnCe_{0.3}Fe_{1.7}O_4$ possesses a higher rate constant than other compositions [55,56]. Hence, spinel $MnCe_{0.3}Fe_{1.7}O_4$ NCs is the optimal attentiveness to enhance the PCD of MB. The rate constant k_{abs} value of MB from the experimental data are given in Table 4.

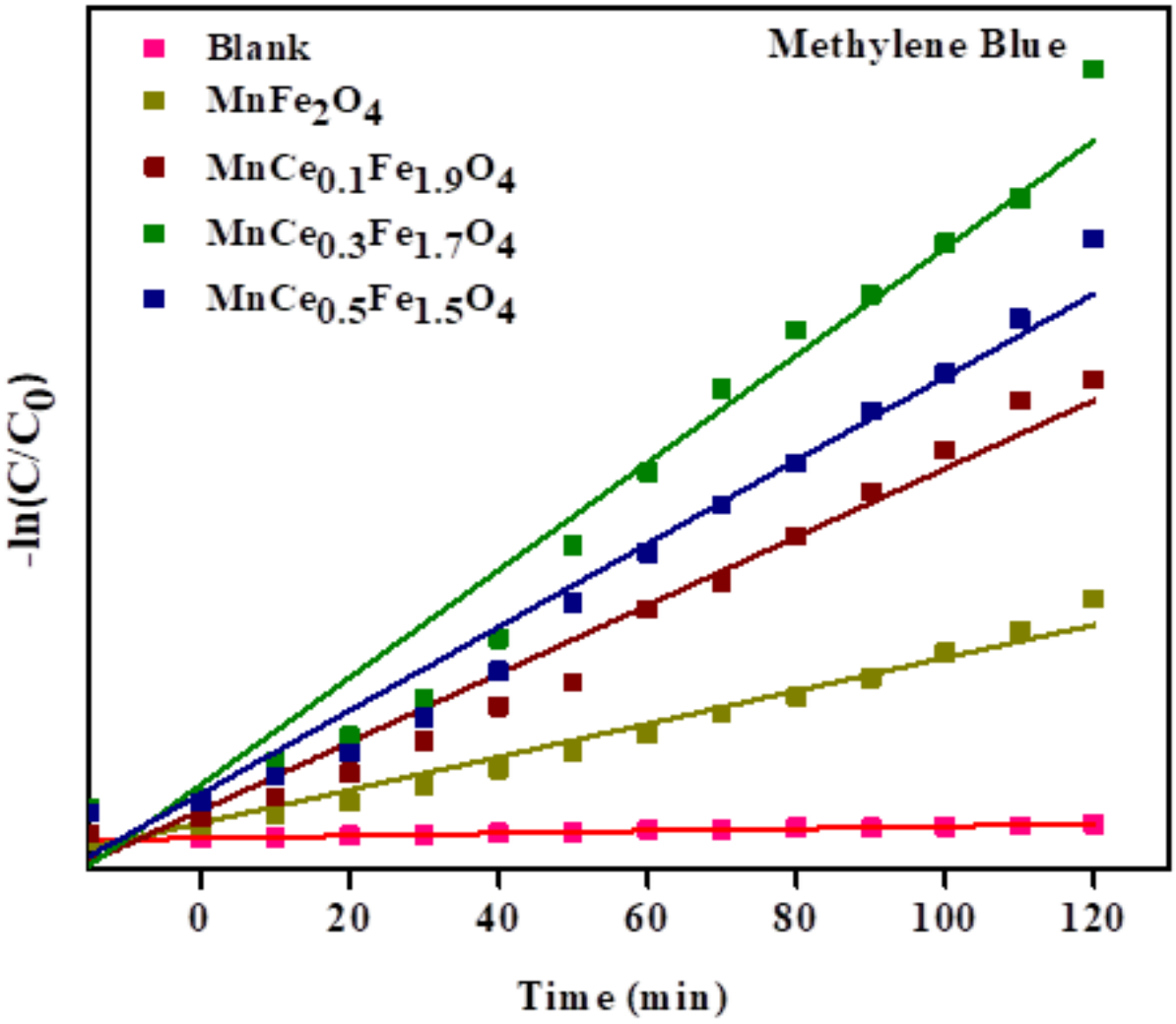


Figure 9. Pseudo-first-order kinetic plot for MB dye degradation using spinel $MnCe_xFe_{2-x}O_4$ (x = 0.0, 0.1, 0.3 and 0.5) NCs.

Table 4. Rate of constant k_{abs} value for the degradation of RhB on spinel $MnCe_xFe_{2-x}O_4$ (x = 0.0, 0.1, 0.3 and 0.5) NCs.

Samples	k min^{-1}				
	Blank	**$MnFe_2O_4$**	**$MnCe_{0.1}Fe_{1.9}O_4$**	**$MnCe_{0.3}Fe_{1.7}O_4$**	**$MnCe_{0.5}Fe_{1.5}O_4$**
MB	0	0.005	0.0126	0.0193	0.0153

3.8. Photocatalytic Degradation Mechanism

Based on the above outcomes, PCD mechanism for MB degradation by Ce doped $MnFe_2O_4$ NCs is shown in Figure 10. When passing through the visible light on the nano-catalysts surface, the electrons, e^-, become excited from the valence band (VB) to the conduction band (CB), along with producing h^+ in VB. The CB excited electrons of $MnFe_2O_4$ NCs become combined cerium and electron–hole (e–h) pair recombination rates become lower, hence the PCD process improves [57–60]. The CB electron becomes combined with a dissolved oxygen molecule to form anions of peroxide radicals ($\bullet O_2^-$) and similarly created •OH, owing to the reaction amongst h^+ and OH− ions. MB decomposes into a simpler molecule in the presence of •OH and $\bullet O_2^-$ species into CO_2 and H_2O. The appropriate PCD mechanism is listed in the following equations:

$$MnCe_xFe_{2-x}O_4 + \text{Visible Light} \rightarrow e^- \text{ (CB)} + h^+\text{(VB)} + \quad (4)$$

$$h^+\text{(VB)} + H_2O \rightarrow H^+ + \bullet OH \quad (5)$$

$$e^- + O_2 \rightarrow \bullet O_2^- \quad (6)$$

$$[\text{MB Dye}] + \bullet O_2^- + \bullet OH \rightarrow H_2O + CO_2 \quad (7)$$

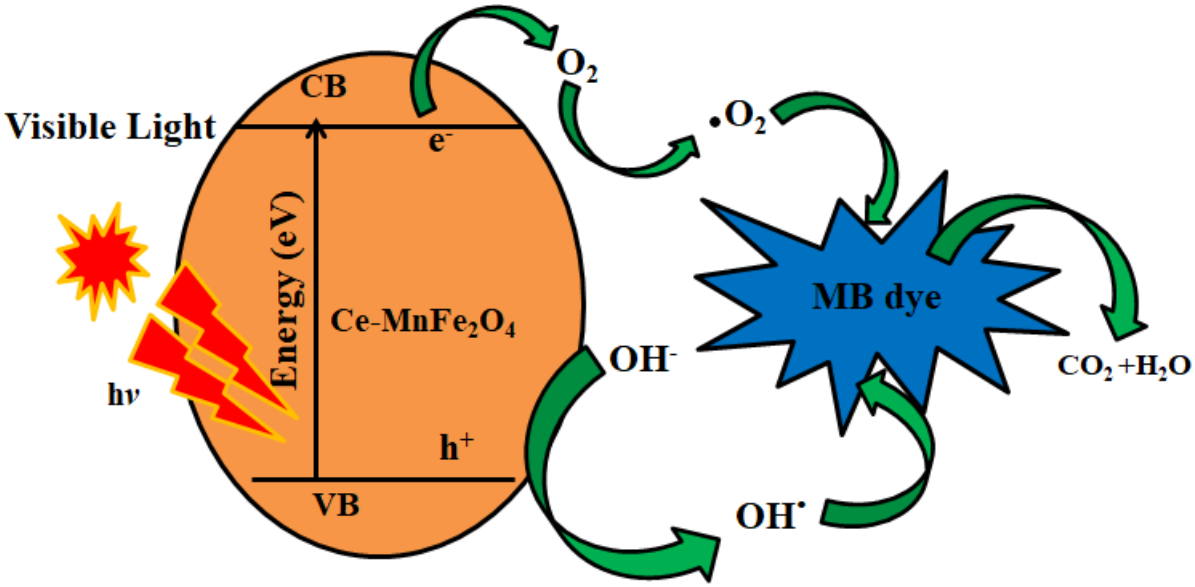


Figure 10. Photo-degradation (PCD) mechanism of MB dye using spinel Ce:$MnFe_2O_4$ NCs.

3.9. Antibacterial Studies

The antibacterial action of $MnFe_2O_4$ and Ce doped $MnFe_2O_4$ NCs (Figure 11) were inspected by the Gram-positive *B. subtilis* and *S. aureus*, and Gram-negative *K. pneumonia* and *E. coli*, which are bacterial strains, correspondingly. It was supposed that there is no region of inhibition found over the control (Figure 11). The antibacterial activity showed that all samples have a positive response in killing bacterial strains. The different concentrations of the samples were used to determine the optimized concentration at which bacterial growth stopped. The measured values of radial diameters of ZOI at varying concentrations are presented in Table 5. The zones of inhibition elucidate that the increase in the concentration of Ce ions leads to a bigger zone of inhibition. The trend was followed: the increasing concentration eventually stops the process of replication and ceases the growth of bacteria. A higher activity can be seen in $MnCe_xFe_{2-x}O_4$ (x = 0.3) NCs compared to the doped and undoped samples. The enhanced antibacterial activity can be defined as the exposure of positively charged ions, such as Ce^{3+}, Fe^{3+}, and Mn^{2+}, which charged bacterial membrane and distorted membrane integrity and can impair electrostatic interaction, leading to the

crossing of membrane barriers, thus disrupting the electron transport chain, and causing cell death. The major element that has played a central role is the ROS species •OH and $•O^{2-}$, and they were higher in $MnCe_xFe_{2-x}O_4$ (x = 0.0, 0.1, 0.3 and 0.5) NCs and the highest in the case of $MnCe_xFe_{2-x}O_4$ (x = 0.3) NCs (evident from photocatalysis). These species have unpaired electrons and can generate oxidative stress and cytotoxicity in the cellular environment. Further, they can start a series of reactions, such as DNA damage, enzyme protein peroxidation, and membrane lipid peroxidation, and inhibit the functioning of the electron's transport mechanism [61,62]. Furthermore, a better attentiveness of Ce ions replacement impact improved antibacterial activity than the smaller Ce exchanged $MnFe_2O_4$ NCs. The smaller grain size and developed surface area with bulk ratio of the products show an exciting atmosphere in antibacterial activity [63,64].

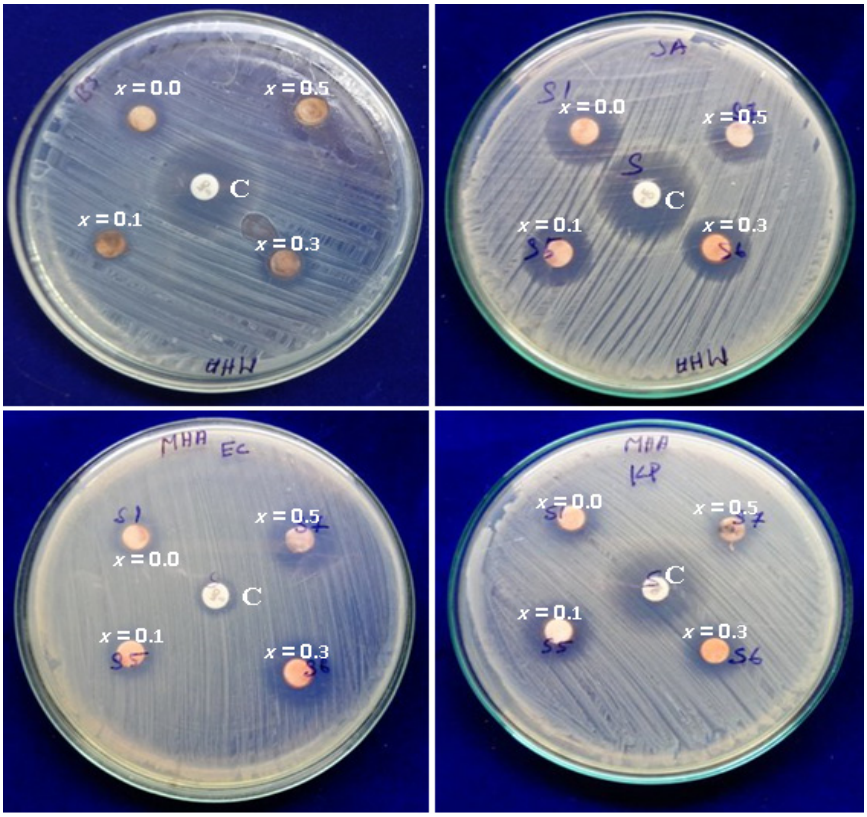


Figure 11. Antibacterial activity of $MnCe_xFe_{2-x}O_4$ (x = 0.0, 0.1, 0.3 and 0.5) NCs.

Table 5. Antibacterial activity of spinel $MnCe_xFe_{2-x}O_4$ (x = 0.0, 0.1, 0.3 and 0.5) NCs.

Bacteria	Zone of Inhibition (mm, Diameter)				
	Control	x = 0.0	x = 0.1	x = 0.3	x = 0.5
B. subtilis	14	12	14	16	16
S. aureus	14	12	14	17	16
E. coli	10	12	14	17	16
K. pneumoniae	16	15	17	20	19

4. Conclusions

Spinel $MnCe_xFe_{2-x}O_4$ NCs were synthesized using manganese nitrate, ferric nitrate, and cerium nitrate, and urea was used as the fuel. In this paper, urea acted as fuel, whereas the precursors of metal nitrates (manganese, ferric and cerium nitrates) functioned as oxidizers. The spinel cubic structure of the sample was confirmed by XRD patterns. Because of lattice distortion, the average crystallite size (nm) shrinks as the concentration of Ce^{3+} rises. Since the particle size decreases as the concentration of Ce^{3+} increases, the PCD

efficiency increases. As a result, these samples could be used to develop photocatalytic materials in the future. According to the VSM analysis, the pure and Ce^{3+} doped $MnFe_2O_4$ NCs shows ferromagnetic behaviour. The photodegradation results exhibited that $MnFe_2O_4$ and Ce doped $MnFe_2O_4$ NCs have the higher potential to degrade methylene blue (MB) and the sample $MnCe_{0.3}Fe_{1.7}O_4$ NCs has shown superb photocatalytic performance (91.53%) than other samples. The antibacterial activities of Gram-positive *S. aureus* and *B. subtilis*, and Gram-negative *K. pneumonia* and *E. coli* were investigated using undoped and Ce^{3+} substituted $MnFe_2O_4$ NCs, and observed a higher activity, which indicated that they can be used in biomedical applications. Additionally, a higher antibacterial activity of Ce^{3+} doped $MnFe_2O_4$ NCs was observed.

Author Contributions: Conceptualization, S.A.A.-Z. and A.M.; methodology, K.T.; software, A.D.; validation, K.K.R., M.A.A. and Y.S.; formal analysis, A.B. and S.B.; investigation, J.A.; resources, S.R.J.; data curation, H.S.A.; writing—original draft preparation, A.M. and M.A.H.; writing—review and editing, A.K.; visualization, I.K.; supervision, A.M.; project administration, A.K.; funding acquisition, S.A.A.-Z. All authors have read and agreed to the published version of the manuscript.

Funding: The Deanship of Scientific Research (DSR) at King Abdulaziz University, Jeddah Saudi Arabia has funded this project, under grant number (KEP-34-130-42).

Institutional Review Board Statement: Not applicable.

Informed Consent Statement: Not applicable.

Data Availability Statement: Not applicable.

Acknowledgments: The Deanship of Scientific Research (DSR) at King Abdulaziz University, Jeddah Saudi Arabia has funded this project, under grant number (KEP-34-130-42). The author Ayyar Manikandan is thankful to Tamil Nadu State Council for Science and Technology (TNSCST), DOTE Campus, Chennai for the financial support (S&T Project: TNSCST/ STP-PRG/AR/2018-2019/9307).

Conflicts of Interest: The authors declare no conflict of interest.

References

1. Waqas, H.; Qureshi, A.; Subhan, K.; Shahzad, M. Nanograin Mn–Zn ferrite smart cores to miniaturize electronic devices. *Ceram. Int.* **2012**, *38*, 1235–1240. [CrossRef]
2. Murugan, E.; Vimala, G. Effective functionalization of multiwalled carbon nanotube with amphiphilic poly(propyleneimine) dendrimer carrying silver nanoparticles for better dispersability and antimicrobial activity. *J. Colloid Interface Sci.* **2011**, *357*, 354–365. [CrossRef] [PubMed]
3. Pubby, K.; Narang, S.B. Influence of grain size and porosity on X-band properties of Mn-Zr substituted Ni-Co ferrites. *Mater. Lett.* **2019**, *244*, 186–191. [CrossRef]
4. Sonia, M.M.L.; Anand, S.; Blessi, S.; Pauline, S.; Manikandan, A. Effect of surfactants (PVB/EDTA/CTAB) assisted sol-gel synthesis on structural, magnetic and dielectric properties of $NiFe_2O_4$ nanoparticles. *Ceram. Int.* **2018**, *44*, 22068–22079. [CrossRef]
5. Murugan, E.; Rangasamy, R. Development of stable pollution free TiO_2/Au nanoparticle immobilized green photo catalyst for degradation of methyl orange. *J. Biomed. Nanotechnol.* **2011**, *7*, 225–228. [CrossRef]
6. Praveena, K.; Sadhana, K.; Bharadwaj, S.; Murthy, S.R. Fabrication of dc–dc converter using nanocrystalline Mn–Zn fer-rites. *Mater. Res. Innov.* **2010**, *14*, 102–106. [CrossRef]
7. Huang, R.; Zhang, D.; Tseng, K.-J. Determination of Dimension-Independent Magnetic and Dielectric Properties for Mn–Zn Ferrite Cores and Its EMI Applications. *IEEE Trans. Electromagn. Compat.* **2008**, *50*, 597–602. [CrossRef]
8. Murugan, E.; Santhoshkumar, S.; Govindaraju, S.; Palanichamy, M. Silver nanoparticles decorated g-C_3N_4: An efficient SERS substrate for monitoring catalytic reduction and selective Hg^2+ions detection. *Spectrochim. Acta Part A Mol. Biomol. Spectrosc.* **2021**, *246*, 119036. [CrossRef]
9. Xie, T.; Li, H.; Liu, C.; Yang, J.; Xiao, T.; Xu, L. Magnetic Photocatalyst $BiVO_4$/Mn-Zn ferrite/Reduced Graphene Oxide: Synthesis Strategy and Its Highly Photocatalytic Activity. *Nanomaterials* **2018**, *8*, 380. [CrossRef] [PubMed]
10. Shen, C.Q.; Ji, H.N.; Wu, J.; Zhu, N.; Niu, J.Q.; Li, H.D.; Niu, X.B. Synthesis and Characterization of MnZn Ferrite Nanoparticles for Biomedical Applications. In Proceedings of the IEEE International Conference on Applied Superconductivity and Electromagnetic Devices (ASEMD), Beijing, China, 15–18 April 2018; pp. 1–2.
11. Anwar, A.; Zulfiqar, S.; Yousuf, M.A.; Ragab, S.A.; Khan, M.A.; Shakir, I.; Warsi, M.F. Impact of rare earth Dy^{+3} cations on the various parameters of nanocrystalline nickel spinel ferrite. *J. Mater. Res. Technol.* **2020**, *9*, 5313–5325. [CrossRef]
12. Shah, J.; Kotnala, R.K.; Singh, B.; Kishan, H. Microstructure-dependent humidity sensitivity of porous $MgFe2O_4$–CeO_2 ce-ramic. *Sens. Actuators B Chem.* **2007**, *128*, 306–311. [CrossRef]

13. Khomskii, D. Multiferroics: Different ways to combine magnetism and ferroelectricity. *J. Magn. Magn. Mater.* **2006**, *306*, 1–8. [CrossRef]
14. Yin, L.; Mi, W. Progress in BiFeO3-based heterostructures: Materials, properties and applications. *Nanoscale* **2020**, *12*, 477–523. [CrossRef] [PubMed]
15. Hou, X.; Wang, X.; Mi, W. Progress in Fe_3O_4-based multiferroic heterostructures. *J. Alloys Compd.* **2018**, *765*, 1127–1138. [CrossRef]
16. Back, M.; Trave, E.; Marin, R.; Marzocco, N.; Cristofori, D.; Riello, P. Energy Transfer in Bi- and Er-Codoped Y_2O_3 Nano-crystals: An Effective System for Rare Earth Fluorescence Enhancement. *J. Phys. Chem. A* **2014**, *118*, 30071–30078.
17. Pal, M.; Brahma, P.; Chakravorty, D. Magnetic and electrical properties of nickel-zinc ferrites doped with bismuth oxide. *J. Magn. Magn. Mater.* **1996**, *152*, 370–374. [CrossRef]
18. Pal, M.; Brahrma, P.; Chakravorty, D. AC conductivity in bismuth oxide doped nickel-zinc ferrites. *J. Phys. Soc. Jpn.* **1998**, *67*, 2847–2851. [CrossRef]
19. Angadi, V.J.; Manjunatha, K.; Kubrin, S.; Kozakov, A.; Kochur, A.; Nikolskii, A.; Petrov, I.; Shevtsova, S.; Ayachit, N. Crystal structure, valence state of ions and magnetic properties of $HoFeO_3$ and $HoFe_{0.8}Sc_{0.2}O_3$ nanoparticles from X-ray diffraction, X-ray photoelectron, and Mössbauer spectroscopy data. *J. Alloys Compd.* **2020**, *842*, 155805. [CrossRef]
20. Sathisha, I.C.; Manjunatha, K.; Angadi, V.J.; Reddy, R.K. Structural, Microstructural, Electrical, and Magnetic Properties of $CuFe_2$-(x + y) $EuxScyO_4$ (where x and y vary from 0 to 0.03) Nanoparticles. *J. Supercond. Nov. Magn.* **2020**, *33*, 3963–3973. [CrossRef]
21. Manjunatha, K.; Angadi, V.J.; Rajaramakrishna, R.; Pasha, U.M. Role of 5 mol% Mg-Ni on the Structural and Magnetic Properties of Cobalt Chromates Crystallites Prepared by Solution Combustion Technique. *J. Supercond. Nov. Magn.* **2020**, *33*, 2861–2866. [CrossRef]
22. Ding, F.; Lin, J.; Wu, T.; Zhong, H. Scanning electron microscopy (SEM), energy-dispersive X-ray (EDX) spectroscopy and nuclear radiation shielding properties of [α-Fe_3+O(OH)]-doped lithium borate glasses. *Appl. Phys. A* **2020**, *126*, 221. [CrossRef]
23. Thakur, P.; Chahar, D.; Taneja, S.; Bhalla, N.; Thakur, A. A review on MnZn ferrites: Synthesis, characterization and applications. *Ceram. Int.* **2020**, *46*, 15740–15763. [CrossRef] [PubMed]
24. Foroutan, R.; Mohammadi, R.; MousaKhanloo, F.; Sahebi, S.; Ramavandi, B.; Kumar, P.S.; Vardhan, K.H. Performance of montmorillonite/graphene oxide/$CoFe_2O_4$ as a magnetic and recyclable nanocomposite for cleaning methyl violet dye-laden wastewater. *Adv. Powder Technol.* **2020**, *31*, 3993–4004. [CrossRef]
25. Boushehrian, M.M.; Esmaeili, H.; Foroutan, R. Ultrasonic assisted synthesis of Kao-lin/$CuFe_2O_4$ nanocomposite for removing cationic dyes from aqueous media. *J. Environ. Chem. Eng.* **2020**, *8*, 103869. [CrossRef]
26. Foroutan, R.; Peighambardoust, S.J.; Esvandi, Z.; Khatooni, H.; Ramavandi, B. Evaluation of two cationic dyes removal from aqueous environments using CNT/MgO/$CuFe_2O_4$ magnetic composite powder: A comparative study. *J. Environ. Chem. Eng.* **2021**, *9*, 104752. [CrossRef]
27. Foroutan, R.; Mohammadi, R.; Ahmadi, A.; Bikhabar, G.; Babaei, F.; Ramavandi, B. Impact of ZnO and Fe_3O_4 magnetic nanoscale on the methyl violet 2B removal efficiency of the activated carbon oak wood. *Chemosphere* **2022**, *286*, 131632. [CrossRef]
28. Foroutan, R.; Peighambardoust, S.J.; Hemmati, S.; Khatooni, H.; Ramavandi, B. Preparation of clinoptilo-lite/starch/$CoFe_2O_4$ magnetic nanocomposite powder and its elimination properties for cationic dyes from water and wastewater. *Int. J. Biol. Macromol.* **2021**, *189*, 432–442. [CrossRef]
29. Sathisha, I.C.; Manjunatha, K.; Bajorek, A.; Babu, B.R.; Chethan, B.; Reddy, T.R.K.; Ravikiran, Y.T.; Angadi, V.J. Enhanced humidity sensing and magnetic properties of bismuth doped copper ferrites for humidity sensor applications. *J. Alloys Compd.* **2020**, *848*, 156577. [CrossRef]
30. Shah, J.; Arora, M.; Purohit, L.; Kotnala, R. Significant increase in humidity sensing characteristics of praseodymium doped magnesium ferrite. *Sens. Actuators A Phys.* **2011**, *167*, 332–337. [CrossRef]
31. Li, Y.; Fan, K.; Ban, H.; Yang, M. Detection of very low humidity using polyelectrolyte/graphene bilayer humidity sensors. *Sensors Actuators B Chem.* **2016**, *222*, 151–158. [CrossRef]
32. Chen, Z.; Lu, C. Humidity Sensors: A Review of Materials and Mechanisms. *Sens. Lett.* **2005**, *3*, 274–295. [CrossRef]
33. Sunilkumar, A.; Manjunatha, S.; Chethan, B.; Ravikiran, Y.; Machappa, T. Polypyrrole–Tantalum disulfide composite: An efficient material for fabrication of room temperature operable humidity sensor. *Sens. Actuators A Phys.* **2019**, *298*, 111593. [CrossRef]
34. Zhang, D.; Wang, D.; Li, P.; Zhou, X.; Zong, X.; Dong, G. Facile fabrication of high-performance QCM humidity sensor based on layer-by-layer self-assembled polyaniline/graphene oxide nanocomposite film. *Sens. Actuators B Chem.* **2018**, *255*, 1869–1877. [CrossRef]
35. Ravinder, D.; Kumar, K.V. Dielectric behaviour of erbium substituted Mn-Zn ferrites. *Bull. Mater. Sci.* **2001**, *24*, 505–509. [CrossRef]
36. Lumina Sonia, M.M.; Anand, S.; Vinosel, V.M.; Janifer, M.A.; Pauline, S.; Manikandan, A. Effect of lattice strain on structure, morphology and magneto-dielectric properties of $NiGdxFe_{2-x}O_4$ ferrite nano-crystallites synthesized by sol-gel route. *J. Magn. Magn. Mater.* **2018**, *466*, 238–251. [CrossRef]
37. Velanganni, S.; Manikandan, A.; Prince, J.J.; Mohan, C.N.; Thiruneelakandan, R. Nanostructured ZnO coated Bi2S3 thin films: Enhanced photocatalytic degradation of methylene blue dye. *Phys. B Condens. Matter* **2018**, *545*, 383–389. [CrossRef]
38. Baykal, A.; Guner, S.; Gungunes, H.; Batoo, K.M.; Amir, M.; Manikandan, A. Magneto Optical Properties and Hyperfine Interactions of Cr^{3+} Ion Substituted Copper Ferrite Nanoparticles. *J. Inorg. Organomet. Polym. Mater.* **2018**, *28*, 2533–2544. [CrossRef]

39. Amir, M.; Gungunes, H.; Slimani, Y.; Tashkandi, N.; El Sayed, H.S.; Aldakheel, F.; Sertkol, M.; Sözeri, H.; Manikandan, A.; Ercan, I.; et al. Mössbauer Studies and Magnetic Properties of Cubic $CuFe_2O_4$ Nanoparticles. *J. Supercond. Nov. Magn.* **2018**, *32*, 557–564. [CrossRef]
40. Slimani, Y.; Güngüneş, H.; Nawaz, M.; Manikandan, A.; El Sayed, H.; Almessiere, M.; Sözeri, H.; Shirsath, S.; Ercan, I.; Baykal, A. Magneto-optical and microstructural properties of spinel cubic copper ferrites with Li-Al co-substitution. *Ceram. Int.* **2018**, *44*, 14242–14250. [CrossRef]
41. Lynda, I.J.C.; Durka, M.; Dinesh, A.; Manikandan, A.; Jaganathan, S.K.; Baykal, A.; Antony, S.A. Enhanced Magneto-optical and Photocatalytic Properties of Ferromagnetic $Mg_{1-y}NiyFe_2O_4$ ($0.0 \leq y \leq 1.0$) Spinel Nano-ferrites. *J. Supercond. Nov. Magn.* **2018**, *31*, 3637–3647. [CrossRef]
42. Esvandi, Z.; Foroutan, R.; Peighambardoust, S.J.; Akbari, A.; Ramavandi, B. Uptake of anionic and cationic dyes from water using natural clay and clay/starch/$MnFe_2O_4$ magnetic nanocomposite. *Surf. Interfaces* **2020**, *21*, 100754. [CrossRef]
43. Amir, M.; Gungunes, H.; Baykal, A.; Almessiere, M.A.; Sözeri, H.; Ercan, I.; Sertkol, M.; Asiri, S.; Manikandan, A. Effect of an-nealing temperature on Magnetic and Mossbauer properties of $ZnFe_2O_4$ nanoparticles by sol-gel approach. *J. Supercond. Nov. Magn.* **2018**, *31*, 3347–3356. [CrossRef]
44. Abraham, A.G.; Manikandan, A.; Manikandan, E.; Vadivel, S.; Jaganathan, S.K.; Baykal, A.; Renganathan, P.S. Enhanced magneto-optical and photo-catalytic properties of transition metal cobalt (Co^{2+} ions) doped spinel $MgFe_2O_4$ ferrite nano-composites. *J. Magn. Magn. Mater.* **2018**, *452*, 380–388. [CrossRef]
45. Ratnayake, S.; Mantilaka, M.; Sandaruwan, C.; Dahanayake, D.; Murugan, E.; Kumar, S.; Amaratunga, G.; de Silva, K.N. Carbon quantum dots-decorated nano-zirconia: A highly efficient photocatalyst. *Appl. Catal. A Gen.* **2019**, *570*, 23–30. [CrossRef]
46. Abraham, A.G.; Manikandan, A.; Manikandan, E.; Jaganathan, S.K.; Baykal, A.; Renganathan, P. Enhanced Opto-Magneto Properties of $NixMg_{1-x}Fe_2O_4$ ($0.0 \leq x \leq 1.0$) Ferrites Nano-Catalysts. *J. Nanoelect. Optoelect.* **2017**, *12*, 1326–1333. [CrossRef]
47. Muthukrishnaraj, A.; Al-Zahrani, S.; Al Otaibi, A.; Kalaivani, S.; Manikandan, A.; Balasubramanian, N.; Bilgrami, A.; Ahamed, M.; Khan, A.; Asiri, A.; et al. Enhanced Photocatalytic Activity of Cu_2O Cabbage/RGO Nanocomposites under Visible Light Irradiation. *Polymers* **2021**, *13*, 1712. [CrossRef]
48. Sri, V.S.P.S.; Manikandan, A.; Mathankumar, M.; Tamizhselvi, R.; George, M.; Murugaiah, K.; Kashmery, H.A.; Al-Zahrani, S.A.; Puttegowda, M.; Khan, A.; et al. Unveiling the photosensitive, mechanical and magnetic properties of amorphous iron nanoparticles with its application towards decontamination of water and cancer treatment. *J. Mater. Res. Technol.* **2021**, *15*, 99–118.
49. Vanitha, M.; Ramachandran, G.; Manikandan, A.; Slimani, Y.; Almessiere, M.A.; Baykal, A.; Dash, C.S. Effect of Sr^{2+} Ion–Substituted Nickel Ferrite Nanoparticles Prepared by a Simple Microwave Combustion Method. *J. Supercond. Nov. Magn.* **2021**, *34*, 971–980. [CrossRef]
50. Vinosha, P.A.; Manikandan, A.; Ceicilia, A.S.J.; Dinesh, A.; Nirmala, G.F.; Preetha, A.C.; Slimani, Y.; Almessiere, M.; Baykal, A.; Xavier, B. Review on recent advances of zinc substituted cobalt ferrite nanoparticles: Synthesis characterization and diverse applications. *Ceram. Int.* **2021**, *47*, 10512–10535. [CrossRef]
51. Vinosha, P.A.; Manikandan, A.; Ragu, R.; Dinesh, A.; Thanrasu, K.; Slimani, Y.; Baykal, A.; Xavier, B. Impact of nickel substitution on structure, magneto-optical, electrical and acoustical properties of cobalt ferrite nanoparticles. *J. Alloys Compd.* **2021**, *857*, 157517. [CrossRef]
52. Vinosha, P.A.; Manikandan, A.; Preetha, A.C.; Dinesh, A.; Slimani, Y.; Almessiere, M.A.; Baykal, A.; Xavier, B.; Nirmala, G.F. Review on recent advances of synthesis, magnetic properties and water treatment applications of cobalt ferrite nanoparticles and nanocomposites. *J. Supercond. Nov. Magn.* **2021**, *34*, 995–1018. [CrossRef]
53. Renuga, R.; Manikandan, A.; Mary, J.A.; Muthukrishnaraj, A.; Khan, A.; Srinivasan, S.; Al Alwan, B.A.M.; Khedher, K.M. Enhanced Magneto-Optical, Morphological, and Photocatalytic Properties of Nickel-Substituted SnO_2 Nano-particles. *J. Supercond. Nov. Magn.* **2021**, *34*, 825–836. [CrossRef]
54. Vinosha, P.A.; Manikandan, A.; Ragu, R.; Dinesh, A.; Paulraj, P.; Slimani, Y.; Almessiere, M.; Baykal, A.; Madhavan, J.; Xavier, B.; et al. Exploring the influence of varying pH on structural, electro-optical, magnetic and photo-Fenton properties of mesoporous $ZnFe_2O_4$ nanocrystals. *Environ. Pollut.* **2021**, *272*, 115983. [CrossRef] [PubMed]
55. TMaksoud, M.A.; Fahim, R.A.; Bedir, A.G.; Osman, A.I.; Abouelela, M.M.; El-Sayyad, G.S.; Abd Elkodous, M.; Mahmoud, A.S.; Rabee, M.M.; Ala'a, H.; et al. Baykal, Nickel sub-stituted $MgFe_2O_4$ nanoparticles via co-precipitation method for photocatalytic applications. *Phys. B Condens. Matter.* **2021**, *606*, 412660.
56. Senthil, R.A.; Osman, S.; Pan, J.; Khan, A.; Yang, V.; Kumar, T.R.; Sun, Y.; Lin, Y.; Liu, X.; Manikandan, A. One-pot preparation of AgBr/α-Ag_2WO_4 composites with superior photocatalytic activity under visible-light irradiation. *Colloid Surf. A Physicochem. Eng. Aspect.* **2020**, *586*, 124079. [CrossRef]
57. Muthukrishnaraj, A.; Kalaivani, S.S.; Manikandan, A.; Kavitha, H.P.; Srinivasan, R.; Balasubramanian, N. Sonochemical syn-thesis and visible light induced photocatalytic property of reduced graphene oxide@ ZnO hexagonal hollow rod nano-composite. *J. Alloys Compd.* **2020**, *83625*, 155377. [CrossRef]
58. Rathinavel, S.; Panda, D.; Manikandan, A. Synthesis and characterization of $MgFe_2O_4$ and $MgFe_2O_4$/rGO nanocomposites for the photocatalytic degradation of methylene blue. *Inorg. Nano-Met. Chem.* **2021**, *51*, 210–217. [CrossRef]
59. Senthil, R.A.; Osman, S.; Pan, J.; Sun, Y.; Kumar, T.R.; Manikandan, A. A facile hydrothermal synthesis of visible-light responsive BiFeWO6/MoS_2 composite as superior photocatalyst for degradation of organic pollutants. *Ceram. Int.* **2019**, *45*, 18683–18690. [CrossRef]

60. George, M.; Ajeesha, T.L.; Manikandan, A.; Anantharaman, A.; Jansi, R.S.; Kumar, E.R.; Slimani, Y.; Almessiere, M.A.; Baykal, A. Evaluation of Cu-$MgFe_2O_4$ spinel nanoparticles for photocatalytic and antimicrobial activates. *J. Phys. Chem. Solids* **2021**, *153*, 110010. [CrossRef]
61. Elayakumar, K.; Manikandan, A.; Dinesh, A.; Thanrasu, K.; Raja, K.K.; Kumar, R.T.; Slimani, Y.; Jaganathan, S.K.; Baykal, A. Enhanced magnetic property and antibacterial biomedical activity of Ce^{3+} doped $CuFe_2O_4$ spinel nanoparticles synthesized by sol-gel method. *J. Magn. Magn. Mater.* **2019**, *478*, 140–147. [CrossRef]
62. Babitha, N.; Priya, L.S.; Christy, S.R.; Manikandan, A.; Dinesh, A.; Durka, M.; Arunadevi, S. Enhanced Antibacterial Activity and Photo-Catalytic Properties of ZnO Nanoparticles: Pedalium Murex Plant Extract-Assisted Synthesis. *J. Nanosci. Nanotechnol.* **2019**, *19*, 2888–2894. [CrossRef] [PubMed]
63. Al-Jameel, S.S.; Rehman, S.; Almessiere, M.A.; Khan, F.A.; Slimani, Y.; Al-Saleh, N.S.; Manikandan, A.; Al-Suhaimi, E.A.; Baykal, A. Anti-microbial and anti-cancer activities of $Mn_{0.5}Zn_{0.5}Dy_xFe_{2-x}O_4$ ($x \leq 0.1$) nanoparticles. *Artif. Cells Nanomed. Biotechnol.* **2021**, *49*, 493–499. [CrossRef] [PubMed]
64. Elayakumar, K.; Dinesh, A.; Manikandan, A.; Palanivelu, M.; Kavitha, G.; Prakash, S.; Kumar, R.T.; Jaganathan, S.K.; Baykal, A. Structural, morphological, enhanced magnetic properties and antibacterial bio-medical activity of rare earth element (REE) Cerium (Ce^{3+}) doped $CoFe_2O_4$ nanoparticles. *J. Magn. Magn. Mater.* **2019**, *476*, 157–165. [CrossRef]